MSFNet: A Network for Lunar Impact Crater Detection Based on Enhanced Feature Fusion with Digital Elevation Model

HE Weidong[1]，LAI Jialong[1,2]，ZHONG Zhicheng[1]，CUI Feifei[1]，XU Yi[2]，ZHANG Xiaoping[2]

（1. School of Science, Jiangxi University of Science and Technology, Ganzhou 341000, China；
2. State Key Laboratory of Lunar and Planetary Sciences, Macau University of Science and Technology, Macau 999078, China）

Abstract：Lunar impact crater detection is crucial for lunar surface studies and spacecraft landing missions, yet deep learning still struggles with accurately detecting small craters, especially when relying on incomplete catalogs. In this work, we integrate Digital Elevation Model (DEM) data to construct a high-quality dataset enriched with slope information, enabling a detailed analysis of crater features and effectively improving detection performance in complex terrains and low-contrast areas. Based on this foundation, we propose a novel two-stage detection network, MSFNet, which leverages multi-scale adaptive feature fusion and multi-size ROI pooling to enhance the recognition of craters across various scales. Experimental results demonstrate that MSFNet achieves an F_1 score of 74.8% on Test Region1 and a recall rate of 87% for craters with diameters larger than 2 km. Moreover, it shows exceptional performance in detecting sub-kilometer craters by successfully identifying a large number of high-confidence, previously unlabeled targets with a low false detection rate confirmed through manual review. This approach offers an efficient and reliable deep learning solution for lunar impact crater detection.

Keywords：object detection；deep learning；impact crater；DEM

Highlights：

- Utilized deep learning techniques to achieve the automatic detection of impact craters in lunar DEM images.
- Incorporated lunar slope features to significantly enhance crater feature representation and dataset quality, thereby providing richer support for the model.
- Developed a two-stage detection network, MSFNet, which employs multi-scale feature fusion and multi-size ROI pooling to effectively improve the model's adaptability and robustness in detecting craters of various scales.

中图分类号：P184　　文献标识码：A　　文章编号：2096-9287(2025)02-0190-15

DOI:10.15982/j.issn.2096-9287.2025.20250010

Reference format: HE W D，LAI J L，ZHONG Z C，et al. MSFNet: a network for lunar impact crater detection based on enhanced feature fusion with digital elevation model[J]. Journal of Deep Space Exploration, 2025, 12 (2) : 190-204.

引用格式：何蔚东，赖嘉龙，钟志成，等. MSFNet：一种利用数字高程模型和增强特征融合的月球撞击坑检测网络[J]. 深空探测学报（中英文），2025，12（2）：190-204.

Introduction

Impact craters are one of the most prominent and standard geological features on the lunar surface. These craters exhibit diverse shapes and extensive distribution, recording the history of celestial impacts that the Moon has endured throughout its long evolutionary process. These impact craters provide crucial evidence for revealing the formation and evolution of the Moon but also serve as an essential basis for studying the impact patterns of extraterrestrial bodies. The physical characteristics of impact craters, such as size, depth, and shape, help scientists infer the timing, energy, and impact range of the events, thus offering insights into the age and geological structure of the lunar surface[1-3]. Additionally, the distribution

收稿日期：2025-02-10　修回日期：2025-03-20

基金项目：National Natural Science Foundation of China (12103020,12363009); Natural Science Foundation of Jiangxi Province (20224BAB211011); Open Project Program of State Key Laboratory of Lunar and Planetary Sciences (Macau University of Science and Technology) (Macau FDCT grant No. 002/2024/SKL); Youth Talent Project of Science and Technology Plan of Ganzhou (2022CXRC9191,2023CYZ26970)

patterns of impact craters are significant for the navigation and path planning of autonomous spacecraft and lunar rovers[4-6]. Accurately identifying and analyzing these geological features can significantly enhance the reliability and efficiency of navigation systems while reducing risks posed by obstacles. In particular, the study of small-diameter impact craters plays a key role in analyzing the formation mechanisms of secondary craters and determining equilibrium diameters in certain regions[7-10]. By accurately identifying these small craters, scientists can better understand the multi-phase processes of impact events, infer the energy distribution during impacts, and trace the propagation paths of shock waves. This is of great scientific value for studying the complex geological evolution of the lunar surface, especially the physical changes triggered by impact events and the mechanisms of secondary crater formation. Therefore, developing efficient and automated techniques for detecting and analyzing impact craters advances planetary science research, supports extraterrestrial exploration missions, and provides critical data for studying small craters and their relationship with secondary craters. This is indispensable for future lunar exploration missions, particularly for detailed investigations of the lunar surface's geological environment.

The statistical study of lunar impact craters has undergone several developmental stages. Early research primarily relied on manual statistical methods. For instance, Head et al. [11]utilized LRO (Lunar Reconnaissance Orbiter) and LOLA (Lunar Orbiter Laser Altimeter) data to generate the first digital terrain model of the Moon, cataloging impact craters with diameters exceeding 20 km, which laid a solid foundation for subsequent studies. Later, Povilaitis et al. [12]extended the statistical range to include craters with diameters greater than 5 km. The same year, Robbins released an updated impact crater catalog, identifying approximately 1.3 million craters with diameters larger than 1 km[13]. While manual methods provide valuable data, they also have significant limitations. Manual annotation is constrained by visual acuity and the experience of the annotators. Small-diameter impact craters are particularly prone to being overlooked in regions with complex terrain or poor lighting conditions. Furthermore, since manual annotation relies heavily on subjective judgment, issues related to consistency and reliability often arise, leading to potential biases in crater catalogs. With advances in image processing technology, traditional image processing methods have been introduced to impact crater detection to address some of the shortcomings of manual approaches[14-16]. However, these methods are computationally expensive and lack adaptability, making it challenging to handle large-scale high-resolution datasets with comprehensive coverage efficiently.

With the rapid advancement of artificial intelligence technologies such as deep learning, lunar impact crater detection and analysis have achieved significant breakthroughs in recent years. Cui et al.[17]based on the YOLOv5 object detection algorithm, conducted automatic identification of impact craters with diameters ranging from 2 to 15 km in the South Pole–Aitken Basin, further demonstrating the advantages of deep learning in crater detection. Additionally, Zhao et al.[18]adopted an improved UNet network for image segmentation, achieving outstanding detection performance. Zou et al.[19]employed a two-stage network, Faster R-CNN, and improved it, achieving efficient detection of impact craters at various scales with excellent results. Miao et al.[20] integrated semi-supervised strategies with deep learning methods, significantly enhancing the recall rate of crater recognition. Furthermore, La Grassa et al.[21] combined super-resolution techniques with YOLOv5, yielding remarkable results in detecting small impact craters. These studies highlight the vast potential of deep learning in the lunar impact crater detection field.

Despite the significant progress in lunar impact crater detection using deep learning, several challenges remain. Variations in data references and crater identification methods across different studies have led to inconsistencies in training data standardization. Currently, most deep learning studies rely on standard datasets provided by Head and Povilaitis et al. However, these datasets have limited annotation coverage for small impact craters, resulting in their underrepresentation in training data. This imbalance in data distribution constrains the model's ability to effectively learn the characteristics of small craters, thereby affecting detection performance, particularly in complex terrains and low-contrast regions. In addition, with the continuous accumulation of multi-source lunar data, how to effectively integrate these data to improve impact crater detection accuracy remains a major

challenge in lunar crater detection. Therefore, enhancing the detection rate of small craters and strengthening the deep learning model's ability to learn features from multi-source data fusion has become a key direction for future research.

To address the challenges above, this study introduces a series of optimization measures to enhance the recall rate of deep learning models and improve their ability to learn features of small-impact craters. First, by systematically analyzing the characteristics of impact craters, a high-quality dataset was constructed to tackle detection challenges in complex regions and low-contrast areas specifically. Second, a novel two-stage object detection network was designed, integrating multi-scale adaptive feature fusion and a multi-size ROI pooling mechanism. This design improves the model's adaptability to craters of varying sizes. It enhances its robustness in complex terrain conditions, thereby reducing missed detections and improving the detection of small impact craters. The main contributions of this study include:

1) High-Quality Dataset Construction: Through analysis, it was observed that impact craters exhibit significant slope variations at their locations. Based on this finding, lunar surface slope features were incorporated into the data construction process to enhance the representation of crater characteristics. Compared to the original DEM data, this method significantly improves the quality of the dataset, enhances its feature representation capability, and thereby provides more comprehensive and reliable feature support for the detection model.

2) Novel Detection Network: A new two-stage object detection network, MSFNet, is proposed to improve the efficiency of feature utilization for impact craters. By incorporating an enhanced feature extraction and fusion mechanism, the proposed MSFNet can more effectively capture the key characteristics of craters. Compared to existing two-stage networks, it demonstrates superior capabilities in feature fusion and feature selection.

3) Multi-Scale Adaptive Feature Fusion Network: A multi-scale adaptive feature fusion network has been developed, which effectively integrates features across different scales through multi-scale adaptive fusion and feature selection based on an attention mechanism. Compared to existing feature fusion networks, it demonstrates superior performance in fusing and selecting features of craters with varying sizes.

4) Multi-Size ROI Pooling Layer: A multi-size ROI pooling layer was designed to prevent the loss of small crater features during multiple convolution operations. Compared to a single-layer ROI pooling layer, this layer more effectively captures and retains the critical features of small craters, thereby ensuring that key information is fully preserved during the final detection stage.

1 Data and Methods

1.1 Data

1.1.1 Data Preparation

In this study, the detection of lunar impact craters is defined as an object detection task, and its performance heavily depends on the dataset's quality. Therefore, constructing a high-quality dataset is a key step in improving the model's performance. To this end, we selected the lunar Digital Elevation Model (DEM) as the data source, as it provides a stable representation of crater features while effectively reducing inconsistencies caused by varying lighting conditions[22]. Specifically, the DEM data used in this study covers a region with a latitude range of ±60° and a longitude range of ±180°, with a resolution of 59 meters per pixel (or 512 pixels per degree)[23]. This resolution is sufficient to capture the terrain details of the lunar surface while avoiding the data processing complexity and computational resource demands associated with higher resolutions. For a scientifically sound model training and evaluation, the global images were divided into four sub-regions for the training, validation, and testing sets, with their specific locations shown in Table 1 and Fig. 1. This partitioning ensures the independence and reliability of model evaluation, providing a solid foundation for the accuracy of the research results.

Table 1 Division of latitude and longitude regions for training, validation, and testing sets

Region	Longitude range/（°W, °E）	Latitude range/（°S, °N）
Train region	(0, 160)	(50, 50)
Val region	(5, 30°)	(5, 20)
Test region1	(32, 44)	(0, 16)
Test region2	(45, 75)	(0, 30)

Selecting an appropriate crater catalog is crucial in constructing a high-quality dataset. Currently, there are

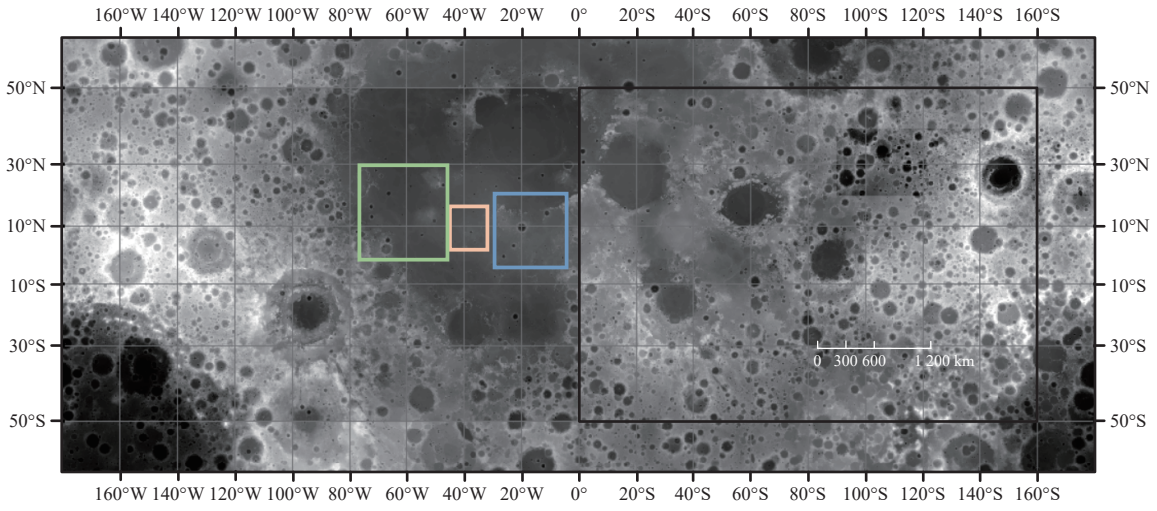

Fig. 1　The division of the training, validation, and test regions on the DEM. The black box represents the Train region, the blue box represents the Val region, the yellow box represents Test region1, and the green box represents Test region2

several lunar impact crater catalogs, primarily categorized into manually curated and automatically generated types. Generally, datasets with more complete annotations and richer details provide more information for deep learning models, significantly improving their training effectiveness and performance. In this regard, the detailed lunar crater catalog published by Robbins et al. is particularly noteworthy. This catalog contains over 2 million crater records generated through a comprehensive analysis of optical remote sensing images and DEM. It provides significant support for studying the distribution and characteristics of lunar impact craters. The catalog includes detailed information on each crater's latitude, longitude, radius, and elliptical radius, with high coverage across craters of different sizes and types. These high-quality and rich data offer a solid foundation for crater detection and analysis, vital in enhancing model performance.

We employed a combination of random and sequential cropping to generate dataset samples to ensure comprehensive sampling[24-25]. By analyzing the diameter distribution of craters in the training set of the Robbins database (as shown in Fig. 2), we observed that many craters have diameters in the range of 1 to 3 kilometers. Based on this distribution, we set the cropping size of the images to 640 pixels, corresponding to an approximate ground coverage of 3.8 km, allowing us to preserve crater details while maintaining processing efficiency. Furthermore, we formatted the generated data set according to the PASCAL VOC standard to ensure fair comparison and evaluation with other models[26]. This standardization enhances the dataset's universality and portability and provides a consistent benchmark for performance comparison across models. The workflow diagram is shown in Fig. 3.

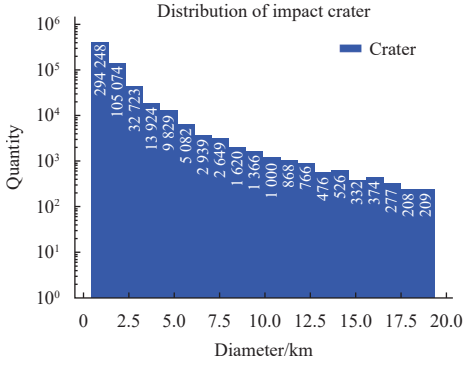

Fig. 2　Distribution of impact craters in the training region

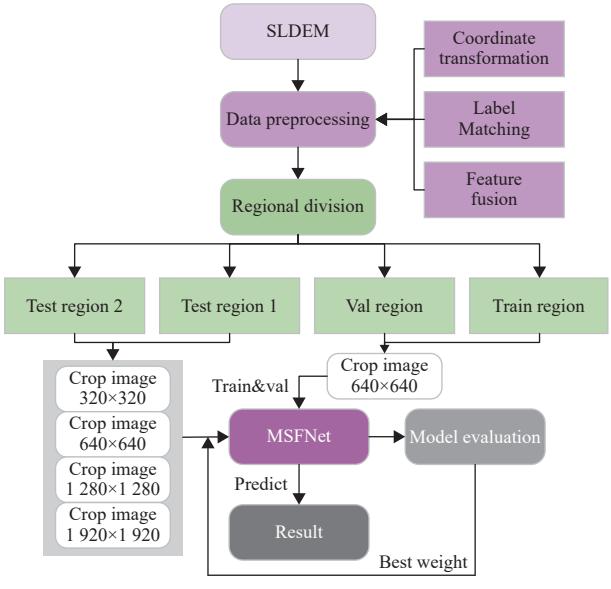

Fig. 3　The flowchart of this study

1.1.2 Data Fusion

In DEM images, the value of each pixel represents the surface elevation at that point relative to the lunar surface. We used DEM data with a resolution of 59 meters per pixel, which comprehensively describes the lunar surface's topography. However, some small impact craters' terrain details are relatively vague, making them difficult for the model to identify. We introduced slope maps as supplementary information to improve the recognition of these small craters. Slope reflects local surface changes, indicating the degree and direction of terrain inclination, and effectively captures the trends in topographical variation. The calculation formula is shown in Equation (1).

$$\theta_s = \arctan\left(\sqrt{\left(\frac{\mathrm{d}z}{\mathrm{d}x}\right)^2 + \left(\frac{\mathrm{d}z}{\mathrm{d}y}\right)^2}\right) \tag{1}$$

The slope map enhances the local terrain variations in the image by calculating the degree of inclination at each point on the surface, especially in complex or low-contrast areas. By fusing the slope map with the original elevation data, we can more effectively highlight the topographical features of the lunar surface. For impact craters, the slope information strengthens the elevation difference at the crater's edge, helping to distinguish the edge from the bottom area, thereby improving the detection accuracy of small craters, particularly in cases where details are blurry. As shown in Fig. 4, the left image is the original, the center is the slope map, and the right image is the result of the fusion of the slope information. For some small craters, the original image may not show enough clarity, while the slope map highlights the terrain structure but lacks the texture details of the original image. By combining both, we not only retain the detailed information of the original image but also incorporate terrain features, significantly enhancing the sensitivity to small impact craters.

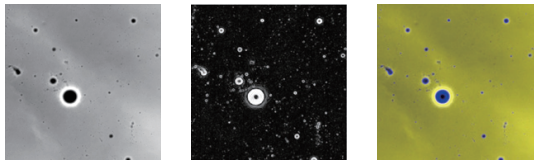

Fig. 4 The original image (a), slope map (b), and the fused feature map (c)

1.2 Methods

1.2.1 MSFNet

We adopted a two-stage network architecture strategy to achieve better performance in lunar impact crater detection and proposed a deep learning model, MSFNet, specifically for lunar impact crater recognition. As shown in Fig. 5, the network consists of a backbone network, a neck network for multi-scale adaptive feature fusion, a Region Proposal Network (RPN), and a head prediction network. We selected ResNet-50 as the backbone network to provide rich multi-scale feature maps[27]. In the neck network, we comprehensively fuse feature maps of different sizes from the backbone to enhance the features' representation capability. To better meet the detection needs of small craters, we designed two ROI Pooling layers in the RPN to retain features of different sizes, enabling more effective learning of crater features. Finally, the model processes the detection results through classification and regression modules.

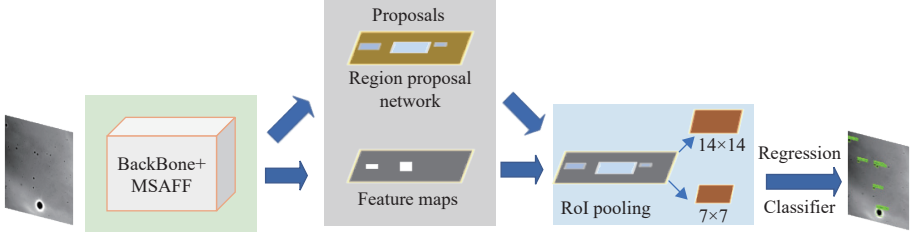

Fig. 5 The MSFNet architecture diagram

Additionally, since most impact craters are close to circular or approximately circular, we set the crater labels as circular. Therefore, we designed 1:1 aspect ratio anchor boxes, which better accommodate the aspect ratio consistency of targets, especially for circular or near-square objects. With this design, the model can more accurately predict the bounding boxes of these targets, thereby reducing localization errors caused by aspect ratio mismatches and improving detection accuracy. Considering the varying sizes of craters, we set anchor boxes at multiple scales,

including 8^2、16^2、32^2、64^2、128^2、256^2 and 320^2, on each feature map to better accommodate craters of different sizes.

1.2.2　Multi Scale Adaptive Feature Fusion Network

In Convolutional Neural Networks (CNNs), shallow features typically contain rich positional information but weak semantic representation, while deep features have a stronger semantic understanding but limited positional information[28]. This separation of features poses a challenge, especially when handling complex tasks, as the network faces limitations in object localization and precise recognition. Shallow features provide accurate positional details but lack sufficient semantic information, making it difficult to understand the overall content of the image entirely. On the other hand, while rich in semantic expression, deep features lose fine positional details, leading to a decline in localization accuracy. Therefore, effectively fusing shallow and deep features to leverage both strengths is a key challenge for improving model performance.

We have independently designed and developed an efficient network architecture specifically for integrating impact crater features, as illustrated in Fig. 6. This network incorporates an Adaptive Spatial Feature Fusion (ASFF) module[29], an attention mechanism module, and a feature pyramid module[30], enabling effective integration of feature information across different scales while minimizing information loss or interference.

The ASFF module integrates feature maps from different scales through an adaptive weighting mechanism, effectively capturing multi-scale information and preventing information loss. Before feeding the input to the ASFF module, we extract four feature maps of varying scales, f_1, f_2, f_3, and f_4, and align their spatial dimensions to ensure consistent spatial resolution.

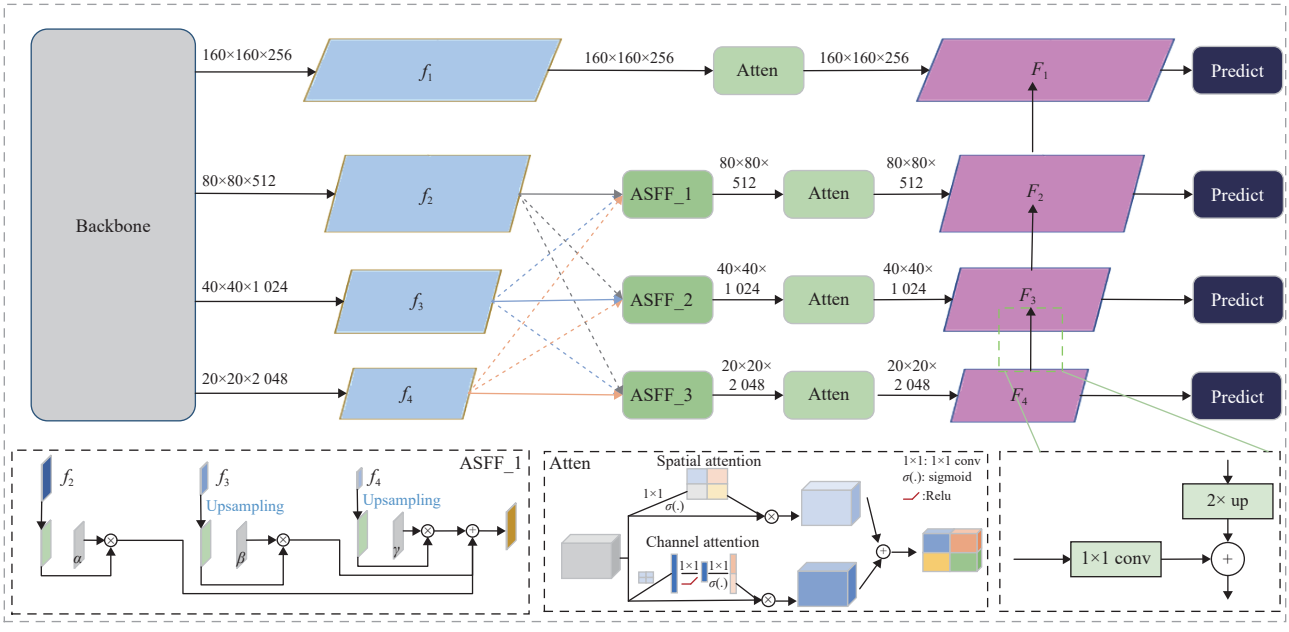

Fig. 6　MSAFF network architecture diagram

Taking the ASFF_1 module as an example, we first apply a 1×1 convolution to the feature map f_3 for channel transformation, then upsampling it to twice the original image resolution, resulting in the feature map X^3. Similarly, we process f_4 with a 1×1 convolution and upsampling it to four times the original resolution, obtaining the feature map X^4. The feature map f_2 remains at its original size, yielding X^2. After aligning the spatial dimensions, we multiply X^2, X^3, and X^4 by the weight parameters α, β, and γ, respectively, and sum the weighted feature maps to produce the fused feature map.

The calculation steps for the weight parameters α, β, and γ are as follows: First, we apply a 1 × 1 convolution to the resized feature maps f_2, f_3, and f_4 to generate new feature maps. These feature maps are then concatenated and normalized using a softmax operation, ensuring that the weights are within the range [0, 1] and their sum equals 1. This process leverages the contextual information

from feature maps of different scales, enhancing the expression capability of multi-scale features and thereby improving the model's performance. Equations (2) and (3) show the detailed calculation process.

$$y_i = \alpha_i X_i^2 + \beta_i X_i^3 + \gamma_i X_i^4 \tag{2}$$

$$\alpha_i = \frac{e^{\lambda \alpha_i}}{e^{\lambda \alpha_i} + e^{\lambda \beta_i} + e^{\lambda \gamma_i}} \tag{3}$$

The fused feature map is then passed through parallel spatial and channel attention modules. This design aims to fully exploit the multi-level information in the feature map to improve detection accuracy. In the channel attention module, the input feature map is first compressed using global average pooling to obtain a feature descriptor with the number of channels. Then, two 1 × 1 convolutional layers are used to capture the relationships between channels and generate the importance weights for each channel. Finally, a channel attention map is obtained through a Sigmoid activation function, representing the importance of each channel in the input feature map. By element-wise multiplication and weighting with the original input feature map, the model can emphasize important channels and suppress unimportant ones, thereby enhancing the representation of key features. In the spatial attention module, the features are first processed through a 1 × 1 convolution operation to generate a single-channel spatial attention map. The weights for each spatial position are derived through a Sigmoid activation function, capturing the importance of spatial positions. This spatial attention map is then element-wise multiplied and weighted with the input feature map to emphasize crucial regions and suppress irrelevant ones. This combination of channel and spatial attention mechanisms enables the network to focus on both important spatial locations and channel features, leading to more accurate impact crater detection in complex environments. In this way, the model not only selects valuable information more effectively but also suppresses the interference of irrelevant or redundant information, thereby improving overall detection performance.

Finally, the optimized feature maps are input into the Feature Pyramid Network (FPN) module. The FPN module efficiently fuses different-level features through top-down feature propagation and bottom-up enhancement. Overall, the proposed Multi Scale Adaptive Feature Fusion (MSAFF) network effectively minimizes feature loss and enhances feature representation, enabling the model to detect impact craters more accurately even in complex backgrounds.

1.2.3 Multi-size ROI Pooling

In deep learning, after multiple convolution operations, the feature information of small objects often gradually fades[30]. This is because convolution operations aggregate information through local receptive fields, and with each convolution layer, the resolution of the feature map decreases, leading to the loss of details and positional information. Specifically, for small objects that occupy fewer pixels, the original fine-grained features can easily be blurred or compressed after passing through multiple convolution layers, affecting object recognition and localization accuracy.

After processing by the multi-scale adaptive feature fusion network, the network generates four feature maps of different sizes, preserving multi-scale information from high to low resolution and providing rich feature support for object detection tasks. In the RPN module, we first generate candidate boxes and map them to the corresponding feature maps to extract key information from the target regions. To mitigate the loss of features for small-sized craters, we designed two sets of ROI pooling layers with different sizes (7×7 and 14×14) to accommodate the feature extraction needs for multi-scale targets, as detailed in Fig. 7. The 7 × 7 ROI pooling layer compresses the spatial dimensions of the feature map, effectively capturing global feature information for large craters while supporting subsequent object classification and regression tasks. However, for small-sized craters, the 7 × 7 ROI pooling layer may excessively compress the feature map, leading to the loss of local detail information, which in turn results in insufficient representation of key features for small craters in subsequent feature expressions, ultimately degrading detection accuracy. To mitigate this issue, we further introduced the 14 × 14 ROI pooling layer, whose larger pooling size retains a broader range of local detail features during compression, thereby preserving features of small craters as much as possible. This approach helps alleviate the problem of feature loss for small craters, improving detection performance. After feature extraction, the feature maps from both the 7 × 7

and 1 4 × 14 ROI pooling layers are flattened into one-dimensional vectors, which are then concatenated to integrate information from different scales, forming a joint feature vector.

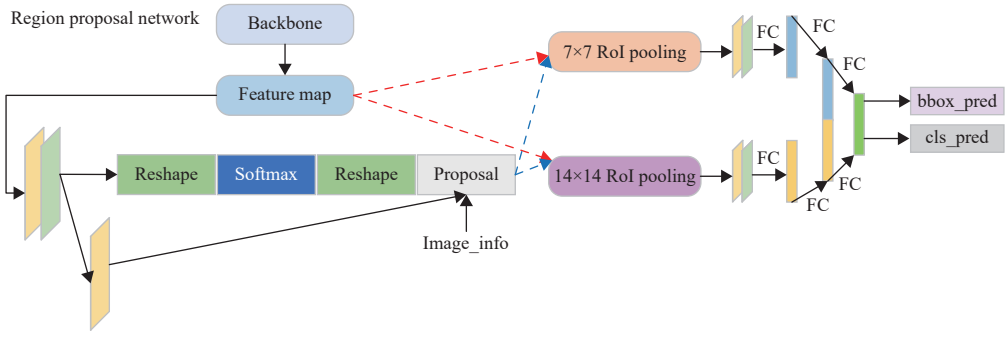

Fig. 7　Design details of multi-size ROI Pooling

Finally, the joint feature vector is passed into a fully connected layer for further feature processing before being fed into the detection head. The network performs object classification and bounding box regression tasks in the detection head. The classification branch is responsible for predicting the object class. In contrast, the regression branch adjusts the position and size of the candidate boxes to obtain precise bounding boxes for the targets.

2　Results

2.1　Experimental Setup

The experiment was implemented using the PyTorch framework, an open-source machine learning tool widely used in academic research and industry, with automatic differentiation capabilities[31]. Regarding hardware configuration, the experiment was conducted on a CentOS7 operating system, and training was carried out using an NVIDIA GeForce RTX 3080Ti GPU. During the model training process, we selected ResNet-50 as the pre-trained network and utilized the SGD optimizer with a learning rate of 0.01, weight_decay of 0.000 1, and a batch size of 8[32]. The training lasted for 40 epochs.

During the model evaluation phase, to determine whether a predicted crater is a valid target, we set the Intersection over Union (IoU) threshold to 0.5 to distinguish between positive and negative samples. In the region prediction stage, we detected craters of four different sizes: 320 × 320, 640 × 640, 1 280 × 1 280 and 1 920 × 1 920. In the post-processing phase, In the post-processing stage, to avoid the duplication of detections for the same crater, we set the IoU threshold to 0.7. If the IoU between two predicted boxes exceeds 0.7, they are considered to correspond to the same target. This strategy effectively eliminates duplicate predictions at different scales, improving the accuracy and reliability of the detection. All models were trained on the same training and validation sets and evaluated on a consistent test set to ensure the comparability and reliability of the results.

2.2　Evaluation Indicators

After training Net on the impact crater training set, we comprehensively evaluated its performance on both the validation and test sets. Traditional evaluation metrics, such as precision, recall, and F_1-score, were used to assess the performance of the impact crater detection algorithm[33].

Precision (P) indicates the degree of consistency between the automatic recognition results and the database, precisely the proportion of samples predicted as impact craters that are impact craters.

$$P = Tp/(Tp + Fp) \tag{4}$$

Recall (R) represents the completeness of the automatic recognition results relative to the database, precisely the proportion of actual impact crater samples successfully predicted as impact craters.

$$R = Tp/(Tp + Fn) \tag{5}$$

The F_1-score is the harmonic mean of precision and recall, comprehensively evaluating the model's detection performance.

$$F_1 = 2 \times P \times R/(P + R) \tag{6}$$

To more accurately assess the model's performance

in impact crater detection and reduce subjective interference, we designed a new evaluation method. This method performs local search matching of the predicted results at corresponding locations in Robbin's impact crater catalog. It compares the detected true positive crater positions with the actual crater locations for precise localization evaluation. This approach effectively reflects the model's localization capability in practical applications. Based on this, we established several evaluation metrics, including radius error ($Error_r$), center x-coordinate error ($Error_x$), and center y-coordinate error ($Error_y$), to comprehensively evaluate the model's performance and its practical value in impact crater detection tasks.

$$Error_r = \frac{1}{N_{\mathrm{TP}}} \sum_{i=1}^{N_{\mathrm{TP}}} |r_i^{\mathrm{pred}} - r_i^{\mathrm{true}}| \tag{7}$$

$$Error_x = \frac{1}{N_{\mathrm{TP}}} \sum_{i=1}^{N_{\mathrm{TP}}} |x_i^{\mathrm{pred}} - x_i^{\mathrm{true}}| \tag{8}$$

$$Error_y = \frac{1}{N_{\mathrm{TP}}} \sum_{i=1}^{N_{\mathrm{TP}}} |y_i^{\mathrm{pred}} - y_i^{\mathrm{true}}| \tag{9}$$

In this context, N_{tp} denotes the number of detected positive samples. The r_i^{pred} and r_i^{true} denote the predicted and ground truth pixel radii of the positive samples, respectively. Similarly, x_i^{pred} and x_i^{true} correspond to the positive samples' predicted and true pixel coordinates along the x-axis. In contrast, y_i^{pred} and y_i^{true} represent the predicted and ground truth pixel coordinates of the positive samples on the y-axis.

2.3 Experimental Analysis

2.3.1 Analysis of Results Under Different Confidence Scores

To comprehensively evaluate the performance of different impact crater detection models at various confidence thresholds, we analyzed several evaluation metrics, including precision, recall, F_1-score, $Error_r$, $Error_x$ and $Error_y$. By adjusting the confidence threshold (ranging from 0.5 to 0.9 in increments of 0.1), we investigate the impact of different confidence levels on model performance. The compared models include the end-to-end detection model DETR[34], the two-stage detection network Faster R-CNN[35], and the one-stage detection networks YOLOv5[36], YOLOX[37], YOLOv8[38], and MSFNet.

The result is shown in Fig. 8. Across different confidence thresholds, the precision of all models generally increases, indicating that higher confidence levels significantly improve prediction accuracy. Notably, YOLOv8 demonstrates outstanding performance across all

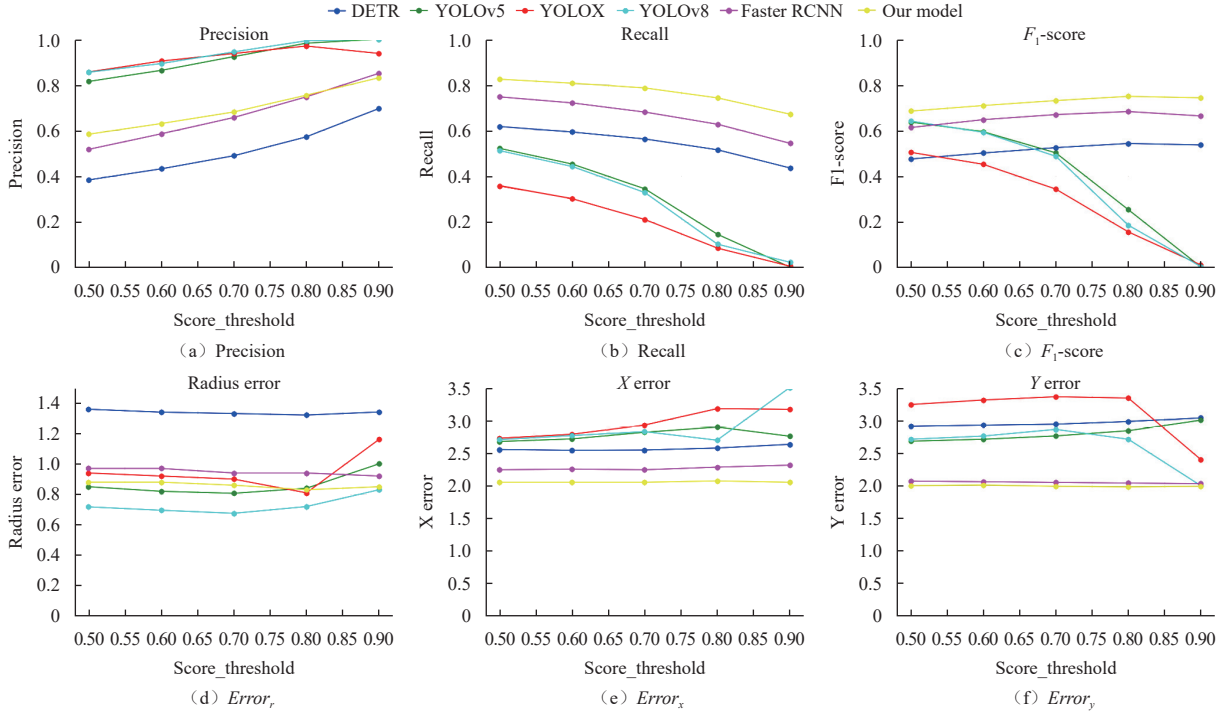

Fig. 8 Comparison of evaluation metrics for different networks at various confidence thresholds

confidence levels. In particular, at a confidence threshold of 0.9, its precision approaches 1, highlighting its superior capability in filtering false positives. However, as the confidence threshold increases, the recall rate of all models tends to decline. At lower confidence levels (0.5–0.6), MSFNet and Faster R-CNN achieve higher recall rates, suggesting their effectiveness in reducing missed detections. Among them, MSFNet stands out with exceptional recall performance, demonstrating high sensitivity and robustness in impact crater detection. As a comprehensive metric balancing precision and recall, the F_1-score provides an overall assessment of model performance across different confidence levels. Experimental results show that MSFNet maintains a consistently high F_1-score across all thresholds, peaking at moderate confidence levels (0.7–0.8). This indicates that MSFNet achieves an optimal trade-off between precision and recall, making it well-suited for practical applications.

In target size estimation, MSFNet exhibits the lowest radius error, demonstrating a clear advantage, whereas DETR shows relatively higher errors. Regarding localization accuracy, MSFNet and Faster R-CNN achieve lower coordinate errors, particularly at mid-to-high confidence thresholds, significantly outperforming other models. This further confirms their strong target localization capabilities in complex scenarios.

Overall, confidence threshold selection has a significant impact on model performance. At low confidence levels (0.5–0.6), recall is higher but precision is lower; at moderate confidence levels (0.7–0.8), an optimal balance between precision and recall is achieved; at high confidence levels (0.9), precision reaches its peak, but recall is notably reduced.

2.3.2　Model Comparison

In Test Region1, we set the model's predicted size to 640x640. We compared its performance with other mainstream object detection models under the evaluation standards of a confidence threshold of 0.8 and an IoU threshold of 0.5. This comprehensive comparative analysis helps assess the model's effectiveness and advantages in practical applications. The experimental results are presented in Table 2 and Table 3, while the visualization of MSFNet's predictions is shown in Fig. 9.

Table 2　Evaluation metrics of different networks on Test Region1 at a confidence threshold of 0.8 and an IoU threshold of 0.5

Model	Precision/ %	Recall/ %	F_1-score/%	$Error_r$/ pixel	$Error_x$/ pixel	$Error_y$/ pixel
Detr	57.30	51.44	54.20	1.32	2.57	2.98
Yolov5	98.20	14.51	25.30	0.84	2.89	2.84
YoloX	96.95	8.47	15.58	0.81	3.17	3.34
Yolov8	99.25	10.18	18.50	0.72	2.69	2.71
Faster R-CNN	74.77	62.61	68.16	0.94	2.28	2.05
Our-model	75.50	74.13	74.80	0.85	2.05	1.99

Table 3　Comparison of predicted and ground truth counts for different networks on Test Region1 at a confidence threshold of 0.8 and an IoU threshold of 0.5

Model	*GT*	*DR*	*Tp*	*Fp*	*Fn*
Detr	2 632	2 363	1 354	1 009	1 278
YOLOv5	2 632	389	382	7	2 250
YOLOX	2 632	270	268	2	2 364
YOLOv8	2 632	230	223	7	2 409
Faster R-CNN	2 632	1 703	1 648	556	984
Our model	2 632	2 584	1 951	633	681

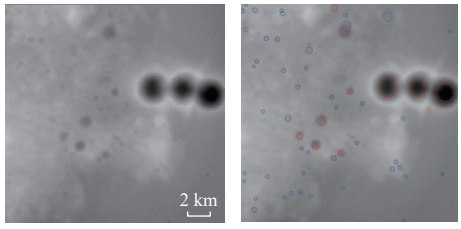

（a）Prediction results of sub-region 1 in Test Region 1

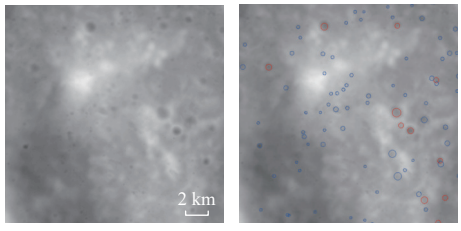

（b）Prediction results of sub-region 2 in Test Region 1

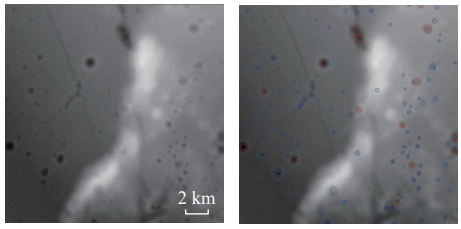

（c）Prediction results of sub-region 3 in Test Region 1

Fig. 9　Visualization results of the MSFNet network on Test Region1. The left side shows the original DEM image, while the right side displays the predicted results. Red indicates correctly detected craters, blue represents newly predicted craters, and yellow highlights missed detections

First, compared to DETR, our model significantly outperforms in Precision, Recall, and F_1-score. Additionally, in error metrics such as $Error_r$, $Error_x$ and $Error_y$, our model demonstrates lower errors, indicating a clear advantage in

target localization and classification accuracy. Notably, our model detects 1 951 true positive samples (*Tp*), while DETR only detects 1 354. This gap further validates the efficiency and accuracy of our model in impact crater detection tasks.

Compared to the YOLO series models (YOLOv5, YOLOX and YOLOv8), our model shows a significant advantage in Recall and F_1-score, especially in Recall, demonstrating stronger performance in reducing false negatives. This is primarily due to the YOLO series models experiencing severely missed detections at high confidence thresholds, resulting in significantly fewer detected true positive samples. For example, YOLOv5 detects only 382 true positives, while our model detects as many as 1 951. Although the YOLO series models perform well in Precision, their high false-negative rate results in a lower F_1 score, failing to balance Precision and Recall.

Compared to Faster R-CNN, our model demonstrates significant advantages across multiple metrics. Precision and Recall have improved, with the F_1-score rising from 68.16% to 74.80%. Additionally, our model is significantly better in error metrics than Faster R-CNN, indicating its higher detection accuracy and more effective reduction of localization errors in impact crater detection tasks. More importantly, our model detects more true positives than Faster R-CNN and has fewer false negatives. These results fully demonstrate the superiority and robustness of our model in impact crater detection tasks.

2.3.3 Comparative analysis of recall rate results

A high recall rate indicates that the model can more comprehensively capture the labeled craters. To evaluate the model's performance, we conducted a recall rate analysis for craters of different diameters on Test Region2 and compared it with the Faster R-CNN model. The experimental results are shown in Table 4. Our model demonstrates excellent performance in crater detection across various diameter ranges, achieving a high recall rate. Specifically, for craters with a diameter greater than 2 kilometers, the recall rate reaches 87.48%, significantly higher than Faster R-CNN's 82.56%. This indicates that our model is more accurate in identifying the majority of actual craters. As the diameter increases, the recall rate remains high, such as 85.66% for craters greater than 3 km and 82.99% for craters greater than 4 km. This further confirms the model's strong detection capability for larger craters, accurately capturing most of the targets. Overall, our model consistently demonstrates a high recall rate across all diameter ranges, particularly excelling in the detection of craters larger than 1 km. This high recall rate significantly reduces the risk of missed detections, providing a solid foundation for comprehensive lunar impact crater detection. The visualization result of MSFNet network on Test Region2 is shown in Fig. 10.

Table 4 Comparison of recall rates for different diameters on Test Region2

Diameter/km	Recall (Our Model)/%	Recall (Faster R-CNN)/%
1–2	76.85	71.23
2–3	84.74	79.85
>2	87.48	82.56
>3	85.66	81.27
>4	82.99	79.54
>5	80.93	76.09

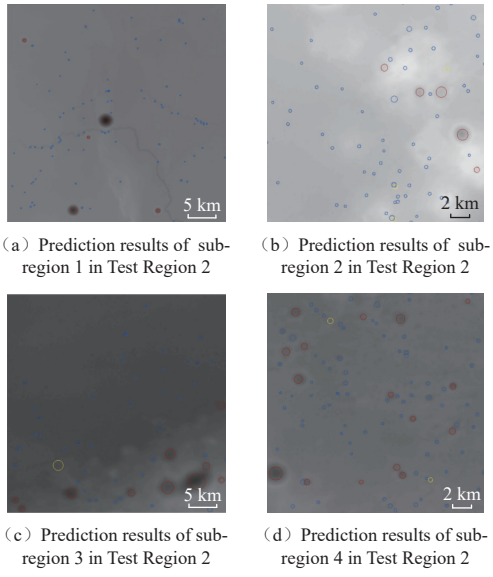

（a）Prediction results of sub-region 1 in Test Region 2
（b）Prediction results of sub-region 2 in Test Region 2
（c）Prediction results of sub-region 3 in Test Region 2
（d）Prediction results of sub-region 4 in Test Region 2

Fig. 10 Visualization results of the MSFNet network on Test Region2. Red represents correctly identified craters, blue indicates newly predicted craters, and yellow highlights missed craters

2.3.4 Exploration of small impact craters

Small targets have always been a challenge in object detection tasks, especially when identifying sub-kilometer craters (with radii around 8 pixels or smaller). These small craters are often difficult for existing crater detection methods to accurately identify, leading to their neglect or omission in catalogs. To address this issue, our model has been specifically optimized for the detection of small craters. In Test Region2 (which contains many small craters not included in the Robbins crater catalog), our model success-

fully identified a large number of small craters. The experimental results are shown in Table 5. The model performed exceptionally well in detecting small craters across different diameter ranges, particularly in the 0.8–1 km and 0.6–0.8 km ranges. Although the number of detections decreased with increasing confidence thresholds, the model still maintained a high detection count at higher confidence levels. For instance, in the 0.6–0.8 km diameter range, even with a confidence threshold greater than 0.99, 9 256 craters were still detected. This demonstrates that our model has strong capabilities in detecting small craters, achieving a high detection rate while improving detection accuracy, especially excelling in the recognition of sub-kilometer craters.

Table 5　Number of detections for different confidence thresholds across various crater diameters

Diameter range/km	Number with confidence >=0.5	Number with confidence >=0.8	Number with confidence >=0.99
0.8-1.0	12 193	8 715	4 195
0.6-0.8	33 835	23 889	9 256
0.4-0.6	33 911	15 277	824

To further validate the performance of the model in detecting sub-kilometer craters on DEM data, we randomly selected two regions in Test Region2 for manual review, with the confidence threshold set to 0.8. To ensure the objectivity and accuracy of the evaluation, we extracted 20% of the crater samples from each selected region for analysis and invited three experts to independently assess the small craters detected by the model. Each expert annotated the misidentified craters within different ranges, and the misidentification statistics from all experts were aggregated to further evaluate the model's detection accuracy. In the evaluation process, we used the False Detection Rate (FDR) as the main evaluation metric. FDR is defined as the proportion of craters detected by the model that were misidentified by the experts. To enhance the reliability of the results, we reported the error using the average ± standard deviation. Table 6 presents the misidentification rate for newly discovered craters. The results show that the MSFNet network had a misidentification rate of approximately 13% in the manual review. Given the resolution limitations of DEM images and the complexity of the detection task, this misidentification rate remains within an acceptable range. Although there was some fluctuation in the misidentification rates for craters of different regions and sizes, the overall performance remained stable, especially for craters with diameters between 0.8 and 1 km, where the misidentification rate was relatively low. This result further confirms the effectiveness and reliability of MSFNet in detecting craters smaller than 1 km on DEM images.

Table 6　Manual review of the prediction results for sub-kilometer craters in Test Region2

Region (Longitude, Latitude)	Diameter range/ km	Total predictions	Randomize samples (20%)	Misidentification counts	FDR/%
Longitude (60°W, 650°W), Latitude (10°N, 15°N)	0.4–0.6	644	128	25 / 23 / 26	19.53±1.18
	0.6–0.8	833	166	23 / 24 / 23	14.26±0.43
	0.8–1.0	210	42	4 / 5 / 6	11.90±2.38
Longitude (55°W, 550°W), Latitude (20°N, 25°N)	0.4–0.6	359	72	11 / 9 / 12	15.74±2.08
	0.6–0.8	653	130	16 / 15 / 17	12.31±0.76
	0.8–0.1	258	52	4 / 3 / 4	7.05±1.08

We conducted a visual analysis of the model's predictions for sub-kilometer craters to provide a more intuitive demonstration of its performance at different confidence levels. In Fig. 11, we use three colors to highlight crater predictions within different confidence intervals: yellow represents craters predicted with a confidence between 0.5 and 0.8, blue indicates craters with a confidence between 0.8 and 0.99, and red corresponds to craters with a confidence exceeding 0.99. The yellow regions with lower confidence indicate potential uncertainty in the model's predictions, typically associated with smaller or more ambiguous craters. In contrast, the blue and red regions with higher confidence predictions reflect the model's high accuracy in recognizing clearer and more prominent craters.

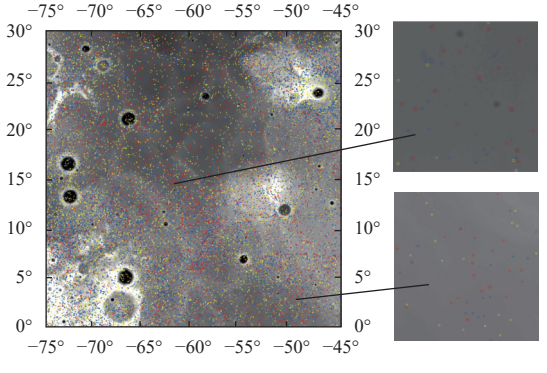

Fig. 11　Visualization of the MSFNet network's predictions for sub-1km craters in Test Region2. Yellow represents craters with confidence between 0.5 and 0.8, blue represents craters with confidence between 0.8 and 0.99, and red indicates craters with confidence greater than 0.99

3 Discussion

3.1 Feature Effectiveness

To investigate the effectiveness of the features, we compared the dataset with integrated slope features against the dataset without slope features using the Faster R-CNN model, evaluating its performance on Test Region1. The experimental results are shown in Table 7. After integrating the slope feature, the model's performance improved across all evaluation metrics. Specifically, Precision increased from 74.77% to 80.64%, Recall rose from 62.61% to 68.38%, and F_1-score increased from 68.16% to 74.01%. These changes indicate that the slope feature significantly enhanced the model's detection accuracy and recall capability. Additionally, while the model with integrated slope features showed a decrease in $Error_r$ (0.822) and $Error_x$ (2.237), $Error_y$ (2.057) slightly increased. The number of craters with a confidence greater than 0.99 (S_{99}) also increased from 753 to 1 002, further validating the positive impact of the slope feature on improving the model's robustness and stability in complex scenarios. Therefore, integrating the slope feature effectively enhanced the model's overall performance in the object detection task, particularly in balancing precision and recall, demonstrating its potential for practical applications.

Table 7 Performance comparison of models with and without Slope features

Model	Precision/%	Recall/%	F_1-score/%	$Error_r$	$Error_x$	$Error_y$	S_{99}
Baseline	74.77	62.61	68.16	0.935	2.278	2.047 9	753
Baseline + slope	80.64	68.38	74.01	0.822	2.237	2.057 0	1 002

3.2 Feature Amplification Strategy

To further enhance the model's crater detection capability, we introduced a feature amplification prediction strategy. Specifically, the input image is first magnified using bilinear interpolation before making predictions, thereby increasing the representation range of target features in the feature map and helping to capture crater characteristics more accurately. The experimental results are shown in Table 8. Under the condition of a confidence threshold of 0.8 and the same test scale, we compared the detection performance with and without the feature magnification strategy in Test Rgion1. After applying the strategy, Recall increased to 76.03%, the number of true positives (Tp) rose to 2001, and the number of false negatives (Fn) decreased to 631, indicating that the strategy effectively enhanced the model's ability to capture targets. However, due to the inclusion of more false positives (Fp) among the newly detected targets, Precision slightly decreased to 71.26%, causing a slight drop in F_1-score to 73.57%. In addition, we present visualizations of the detection results across different confidence levels and diameter ranges, as shown in Fig. 12.

Table 8 Performance comparison of models with and without Feature Amplification strategy

Model	Precision/%	Recall/%	F_1-score/%	Tp	Fp	Fn
Baseline	75.50	74.13	74.80	1 951	633	681
Baseline + FA	71.26	76.03	73.57	2 001	807	631

This result demonstrates that the feature magnification prediction strategy significantly improved the visibility and detection rate of craters by enlarging the input image, enabling the model to detect more craters that were previously undetected. Although the number of false positives increased, the overall recall and crater detection capability of the model were significantly improved, providing an effective technical approach for tackling more complex detection scenarios. In the future, we will further optimize the feature magnification strategy and apply it during the network training process to continuously enhance the model's overall performance and stability.

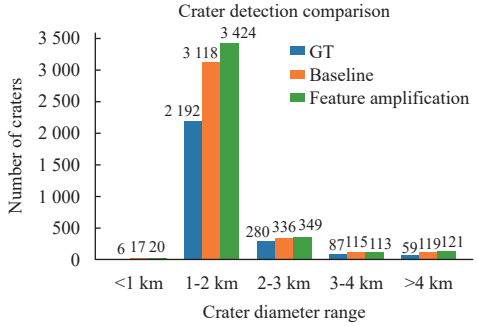

（a）Results at confidence level 0.5

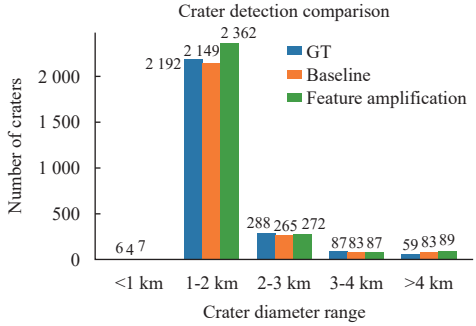

（b）Results at confidence level 0.8

图 12 Comparative analysis of the impact of feature amplification strategy on crater detection performance

4 Conclusion

In this study, we propose MSFNet, an efficient neural network model for lunar impact crater detection. By transforming the crater detection task into a deep learning-based object detection problem, MSFNet introduces two key innovative modules: the Multi-Scale Adaptive Feature Fusion Network (MSAFF) and the multi-size ROI Pooling Layer. The MSAFF module dynamically integrates feature maps from different scales, effectively enhancing the expression capability of crater features and ensuring the complete fusion of detailed and semantic information. The Multi-Size ROI Pooling Layer addresses targets of varying sizes, preserving fine-grained features through 7 × 7 and 14 × 14 pooling operations, providing more diverse features for subsequent classification and regression tasks. The combination of these modules reduces the miss-detection rate and significantly improves the overall detection accuracy, particularly in detecting small impact craters.

Moreover, we effectively integrated the slope features of the lunar surface with the original image features, constructing a more enriched dataset suitable for deep learning models. This dataset retains the fundamental morphological characteristics of the craters while introducing local topographic slope information, providing the model with richer contextual information and further enhancing the accuracy of crater detection.

In the future, our research will focus on the following three areas:

1) Further optimizing crater detection accuracy by adopting higher-resolution DEM data or multi-source data fusion techniques;

2) Applying the model to crater detection tasks on other planets (such as Mars) based on transfer learning, exploring its applicability on different planetary surfaces;

3) Conducting more in-depth research on feature amplification strategies to enhance the model's detection capability in complex scenarios, particularly in challenging terrains and environmental conditions.

References

[1] OUYANG Z Y, LI C L, LIU J Z. Introduction to lunar science[M]. Beijing: Science Press, 2005.

[2] LIU J Z, OUYANG Z Y. Research progress on lunar impact craters[J]. Advance in Earth Science，2007，22(5)：457-465.

[3] ZHANG Z B, LI C L, WANG J T. Morphological characteristics and geological significance of lunar surface impact craters[J]. Geological Science and Technology Information，2021，40(3)：1-10.

[4] LIU A，CHEN M，PAN W. Crater detection algorithm with part PHOG features for safe landing[C]//Proceedings of International Conference on Systems and Informatics (ICSAI2012). [S. l.]：IEEE，2012，103-106.

[5] MAASS B，WOICKE S，OLIVEIRA W M，et al. Crater navigation system for autonomous precision landing on the Moon[J]. Journal of Guidance，Control，and Dynamics，2020，43(8)：1414-1431.

[6] MARTIN I，PARKES S，DUNSTAN M. Modeling cratered surfaces with real and synthetic terrain for testing planetary landers[J]. IEEE Transactions on Aerospace and Electronic Systems，2014，50(4)：2916-2928.

[7] DUNDAS C M，MCEWEN A S. Rays and secondary craters of Tycho[J]. Icarus，2007，186(1)：31-40.

[8] PLESCIA J B，ROBINSON M S. Giordano Bruno：small crater populations—implications for self-secondary cratering[J]. Icarus，2019，321：974-993.

[9] GAULT D E. Saturation and equilibrium conditions for impact cratering on the lunar surface：criteria and implications[J]. Radio Science，1970，5(2)：273-291.

[10] XIAO Z，WERNER S C. Size‐frequency distribution of crater populations in equilibrium on the Moon[J]. Journal of Geophysical Research：Planets，2015，120(12)：2277-2292.

[11] HEAD III J W，FASSETT C I，KADISH S J，et al. Global distribution of large lunar craters：implications for resurfacing and impactor populations[J]. Science，2010，329(5998)：1504-1507.

[12] POVILAITIS R Z，ROBINSON M S，VAN DER BOGERT C H，et al. Crater density differences：exploring regional resurfacing，secondary crater populations，and crater saturation equilibrium on the Moon[J]. Planetary and Space Science，2018，162：41-51.

[13] ROBBINS S J. A new global database of lunar impact craters> 1–2 km：1. Crater locations and sizes，comparisons with published databases，and global analysis[J]. Journal of Geophysical Research：Planets，2019，124(4)：871-892.

[14] XIE Y，TANG G，YAN S，et al. Crater detection using the morphological characteristics of Chang'E-1 digital elevation models[J]. IEEE Geoscience and Remote Sensing Letters，2013，10(4)：885-889.

[15] LIU D，CHEN M，QIAN K，et al. Boundary detection of dispersal impact craters based on morphological characteristics using lunar digital elevation model[J]. IEEE Journal of Selected Topics in Applied Earth Observations and Remote Sensing，2017，10(12)：5632-5646.

[16] ZUO W，ZHANG Z，LI C，et al. Contour-based automatic crater recognition using digital elevation models from Chang'E missions[J]. Computers & Geosciences，2016，97：79-88.

[17] CUI X，DING M，WANG G. Automated crater detection on the South Pole- Aitken basin of the Moon and absolute model ages of mid- sized craters based on convolution neural network[J]. Journal of Nanjing Forestry University (Natural Sciences Edition) ，2021，57：905-915.

[18] ZHAO Y，YE H. Squnet：an high-performance network for crater detection with dem data[J]. IEEE Journal of Selected Topics in Applied Earth Observations and Remote Sensing，2023, 16: 8577-8585.

[19] ZOU C，LAI J，LIU Y，et al. Small lunar crater identification and age estimation in Chang'e-5 landing area based on improved Faster R-

CNN[J]. Icarus，2024，410：115909.

[20] MIAO D，YAN J，TU Z，et al. LCDNet：an innovative neural network for enhanced lunar crater detection using DEM data[J]. IEEE Journal of Selected Topics in Applied Earth Observations and Remote Sensing，2024, 17: 11034-11049.

[21] LA GRASSA R，CREMONESE G，GALLO I，et al. YOLOLens：a deep learning model based on super-resolution to enhance the crater detection of the planetary surfaces[J]. Remote Sensing，2023，15(5)：1171.

[22] SILBURT A，ALI-DIB M，ZHU C，et al. Lunar crater identification via deep learning[J]. Icarus，2019，317：27-38.

[23] BARKER M K，MAZARICO E，NEUMANN G A，et al. A new lunar digital elevation model from the Lunar Orbiter Laser Altimeter and SELENE terrain camera[J]. Icarus，2016，273：346-355.

[24] LEE C. Automated crater detection on Mars using deep learning[J]. Planetary and Space Science，2019，170：16-28.

[25] ZHONG Z C，LAI J，ZHONG Y Q，et al. Enhancing lunar DEM data using super-resolution techniques and optimizing the faster R-CNN network for sub-kilometer crater detection[J]. Icarus，2025, 430: 116483.

[26] EVERINGHAM M，VAN GOOL L，WILLIAMS C K I，et al. The pascal Visual Object Classes (VOC) challenge[J]. International Journal of Computer Vision，2010，88：303-338.

[27] KOONCE B. Convolutional neural networks with swift for tensorflow：image recognition and dataset categorization[M]. Berkeley, CA: Apress, 2021：63-72.

[28] ZEILER M D，FERGUS R. Visualizing and understanding convolutional networks[C]//Proceedings of Computer Vision–ECCV 2014：13th European Conference. Zurich，Switzerland: [s. n.]: 2014.

[29] LIU S，HUANG D，WANG Y. Learning spatial fusion for single-shot object detection[J]. arXiv preprint arXiv：1911.09516，2019.

[30] LIN T Y，DOLLÁR P，GIRSHICK R，et al. Feature pyramid networks for object detection[C]//Proceedings of the IEEE Conference on Computer Vision and Pattern Recognition. [S. l.]: IEEE, 2017: 2117-2125.

[31] PRAKASH K B，KANAGACHIDAMBARESAN G R. Programming with TensorFlow：solution for edge computing applications[EB/OL]. [2025-02-10]. https://doi.org/10.1007/978-3-030-57077-4_10.

[32] RUDER S. An overview of gradient descent optimization algorithms[J]. arXiv preprint arXiv：1609.04747，2016.

[33] LIU Y，LAI J，XIE M，et al. Identification of lunar craters in the Chang'e-5 landing region based on Kaguya TC morning map[J]. Remote Sensing，2024，16(2)：344.

[34] CARION N，MASSA F，SYNNAEVE G，et al. End-to-end object detection with transformers[C]//Proceedings of European Conference on Computer vision. Cham：Springer International Publishing，2020：213-229.

[35] REN S，HE K，GIRSHICK R，et al. Faster R-CNN：towards real-time object detection with region proposal networks[J]. IEEE Transactions on Pattern Analysis and Machine Intelligence，2016，39(6)：1137-1149.

[36] ZHU L，GENG X，LI Z，et al. Improving YOLOv5 with attention mechanism for detecting boulders from planetary images[J]. Remote Sensing，2021，13(18)：3776.

[37] MU L，XIAN L，LI L，et al. YOLO-Crater model for small crater detection[J]. Remote Sensing，2023，15(20)：5040.

[38] BANDYOPADHYAY Y. Lunar crater detection using YOLOv8 deep Learning[EB/OL]. [2025-02-10]. https://doi.org/10.31223/X5J69V.

The Author Profiles

HE Weidong (1999−), male, with research interests in computer vision.

LAI Jialong (1988−), male, Professor, with research interests encompassing artificial intelligence, signal processing, and remote sensing technology for lunar and planetary exploration. His work involves theoretical modeling, numerical simulation, data analysis, and the application of geophysical parameter inversion in planetary science.

Corresponding author of this article.

Address: School of Science, Jiangxi University of Science and Technology (341000)

E-mail: laijialong@jxust.edu.cn

MSFNet：一种利用数字高程模型和增强特征融合的月球撞击坑检测网络

何蔚东[1]，赖嘉龙[1,2]，钟志成[1]，崔飞飞[1]，徐　懿[2]，张小平[2]

（1. 江西理工大学 理学院，赣州 341000；

2. 澳门科技大学 月球与行星科学国家重点实验室，澳门 999078）

摘　要：月球撞击坑检测对月表研究和探测器着陆至关重要，但深度学习在小坑检测上仍存在精度不足的问题，尤其依赖不完整目录时更显挑战。结合DEM数据，构建了融入坡度信息的高质量数据集，深入解析撞击坑特征，从而有效提升复杂地形及低对比度区域的检测性能。基于此，提出了新型两阶段检测网络MSFNet，通过多尺度自适应特征融合和多尺寸ROI Pooling，有效提高了不同尺度撞击坑的识别率。实验表明，MSFNet在测试区域1中F_1达74.8%，直径大于2 km的坑召回率达87%，在亚千米级小坑检测中同样表现突出，成功补充大量高置信度未标记目标，经人工审核误检率低。该方案为月球撞击坑检测提供了高效可靠的深度学习解决思路。

关键词：目标检测；深度学习；DEM；撞击坑

[责任编辑：宋宏，英文审校：宋利辉]